Scientia Iranica B (2011) 18 (6), 1277–1286

Sharif University of Technology

Scientia Iranica

Transactions B: Mechanical Engineering

www.sciencedirect.com

Investigation of the pressure distribution and transition point over a swept wing

M.R. Soltani *, **K. Ghorbanian**, **M. Masdari**

Department of Aerospace Engineering, Sharif University of Technology, Tehran, P.O. Box 1458889694, Iran

Received 4 April 2011; revised 5 September 2011; accepted 3 October 2011

KEYWORDS

Boundary layer;
Spectral analysis;
Instability mode;
Swept wing;
Transition.

Abstract A series of wind tunnel tests are performed to examine the flow field over a swept wing under various conditions. The wing has a laminar flow airfoil section, similar to those of the NACA 6-series. Static pressure distributions over the upper surface of the wing, in both chordwise and spanwise directions, are measured at different angles of attack. The data is employed to predict the transition point at each chordwise section. The skewness parameter of the pressure data shows that this factor drops to zero in the transition region. A comparison of the calculated transition point on the wing surface with that obtained from the 2D computational method shows reasonable agreement over a portion of the model. The power spectral density calculated from the total pressure data of the boundary layer, over the wing surface, at several locations shows the instability modes.

1. Introduction

The knowledge of laminar to turbulent transition phenomenon is of critical importance in many engineering fields, especially in aircraft wing design. The transition not only affects skin friction and flow separation, hence aerodynamic forces, but also has a significant impact on the heat and mass transfer. It should be mentioned that the low skin-friction coefficient of a laminar boundary layer flow is attractive for designing high performance aircraft. In general, all high speed aircraft employ swept wings; thus it is very important to have a laminar boundary layer over the wing surface as large as possible. Further, it is vital to be able to predict the boundary layer transition region over the wing surface, as well as its variations with operational parameters such as angle of attack, Reynolds number, etc.

* Corresponding author.
E-mail address: msoltani@sharif.edu (M.R. Soltani).

1026-3098 © 2012 Sharif University of Technology. Production and hosting by Elsevier B.V. Open access under CC BY license.
Peer review under responsibility of Sharif University of Technology.

doi:10.1016/j.scient.2011.10.001

Production and hosting by Elsevier

A fundamental characteristic of the swept wing boundary layer is the combined effect of the wing sweep angle and the pressure gradient, which produces curved streamlines at the boundary layer edge. While inside the boundary layer, the velocity is reduced and the pressure gradient relative to the external flow is invariant, the resulting imbalance of the pressure gradient produces a cross flow that is perpendicular to the streamline [1].

Ray-Sing indicates that "Boundary layer instability in two-dimensional flows, such as that of the unswept wing, is only related to Tollmien–Schlichting (TS) waves. However, the stability problem is aggravated for the swept wing. The transition process in the three-dimensional boundary layer on a swept-wing typically involves one or more of the following phenomena":

- Attachment-line instabilities and contamination;
- Cross flow vortices: stationary and non-stationary;
- Streamwise instabilities (i.e. TS waves);
- Centrifugal instabilities.

Gray [2,3] initiated one of the first experiments on transition measurement over a swept wing. He observed that the boundary layer of a swept wing becomes turbulent and much closer to the leading edge, compared to an unswept wing under similar conditions. This discovery gave rise to the classical basic research done by Gregory et al. [4]. They revealed the instability mechanism as an inflectional instability due to the cross flow. Basic experimental investigations on swept wing

Nomenclature

V_∞	Freestream velocity (m/s)
C_p	Pressure coefficient $\frac{P-P_\infty}{q_\infty}$
P_0	Local total pressure (N/m^2)
P_∞	Wind tunnel static pressure
q_∞	Dynamic pressure $\frac{1}{2}\rho_\infty V_\infty^2$
ρ_∞	Air density (kg/m^3)
Re	Reynolds number $\frac{\rho_\infty V_\infty C}{\mu}$
C	Airfoil chord (m)
C_r	Wing root chord (m)
C_t	Wing tip chord (m)
$\overline{C}$	Wing average chord $\frac{C_t+C_r}{2}$
μ	Air viscosity

Abbreviation

A.O.A.	Angle Of Attack°
L.E.	Leading Edge
T.E.	Trailing Edge
TS	Tollmien–Schlichting waves
PSD	Power Spectrum Density

transition flows were performed by Poll [5] and, Arnal and Casalis [6] on a swept cylinder, and Michel et al. [7] on a swept flat plate. These experiments confirmed the physical explanation of the instability in the accelerated region of the swept wing flow, as derived by Stuart for flow over a rotating disk [4]. A rather complete review of the work on the stability of three-dimensional accelerated boundary layer flow is given by, White and Saric [8], Saric and Reed [9]. In 1990, a comprehensive experimental study at NASA Langley Research Center was conducted on F-14A variable swept wings modified for laminar flow, to study the transition location under various conditions [10]. The results showed the influence of cross-flow and TS instabilities, along with the effect of wing sweep, on the boundary layer transition region. Further, Kachanov developed techniques to create controlled traveling waves within the boundary layer and observed the growth of these waves [11]. Arnal et al. showed that linear methods are not appropriate in correlating transition for the cross flow-dominated boundary layers [12]. White and Saric also showed that mode selection is the most important feature of the receptivity phase of transition, and depends on both turbulence intensity and surface roughness [13]. Recently, researchers employed spectral analysis of the output signals of various sensors to analyze flow field over a wing surface (pressure, hot wire, etc.), and to examine boundary layer instability [14,15].

The present experimental work aspires to further expand our knowledge of boundary layer transition mechanisms over a swept wing. For this purpose, surface pressure orifices are employed on a swept wing at three different spanwise locations, in conjunction with a boundary layer rake, equipped with high sensitive Kulite pressure sensors installed at the end of each probe. The rake is placed around the mid chord, $\frac{x}{c} = 0.5$, of the wing. Spectral and statistical analyses are used to investigate the instability modes of the boundary layer over the wing surface. Thus, using the knowledge of boundary layer evolution over a swept wing, from its origin at the leading edge to transitional breakdown to turbulence, it is hoped that effective techniques will be identified, which may lead to future flow control strategies. Further, it is believed that these investigations, along with other findings, will enhance the employment of techniques for delaying transition, resulting in reduced drag, less fuel consumption, better maneuverability and safer flight, in general [15].

2. Experimental apparatus

All experiments are conducted in a subsonic wind tunnel of a closed return type with a test section size of $80\times 80\times 200$ cm, operating at speeds ranging from 10 to 100 m/s. The inlet of the tunnel has a 7:1 contraction ratio with four large anti-turbulence screens and a honeycomb in its settling chamber to reduce tunnel turbulence to less than 0.1% in the test section.

The model used in this paper is a scaled model of a tapered wing whose section is similar to that of NACA6-series airfoils. A half model is designed and fabricated to achieve higher Re numbers during the tests. A flat plate is used at the end of the model to reduce the boundary layer effect of the test section on the model.

The general arrangement of the model used for this investigation, when installed in the wind tunnel, is shown in Figure 1. The baseline configuration is a semi-span, 1/2.5 scale model of the actual wing. The model has a leading edge sweep of 23° and a span of 516 mm. The wing upper surface is covered with a total of 90 pressure orifices of 0.4 mm diameter, arranged in three streamwise rows; Section a ($\frac{2y}{b} = 0.2$), Section b ($\frac{2y}{b} = 0.44$), Section c ($\frac{2y}{b} = 0.78$), and one in the spanwise section at $\frac{x}{c} = \frac{1}{4}$ (Figure 1(b) and (c)).

Flow field and boundary layer measurements are performed via a special rake designed and fabricated to minimize blockage and interface effects. As illustrated in Figure 2(a), the rake tubes are bent at an angle of 45° in order to reduce the influence of the rake main body on the flow field over the wing surface. High frequency pressure sensors with a frequency response of 30 kHz are placed at the end of each probe. All transducer data is collected via a terminal board and transferred to the computer through a 64 channel, 12-bit Analog-to-Digital (A/D) board, capable of an acquisition rate of up to 500 kHz. Figure 2(b) shows the rake position over the model surface, both chordwise and spanwise, indicated by lines 1 through 4, where the boundary layer data are collected.

Raw data are digitally filtered, using a low-pass filtering routine. During the filtration process, cut-off frequencies are calculated from either the power spectrum estimation or frequency domain analysis. The advantage of this method is that the noise, which may dominate the signal in the time domain, appears only as a single peak or spike in the frequency domain [16]. Once the frequency of the noise is determined, it is easily filtered out and a clean signal can be obtained for the analysis. Figure 3 shows an example of the PSD for one of the channels, which is also used to identify the cut-off frequency from the spectrum of the white noise. The cut-off frequency for this signal is about 180 Hz, Figure 3.

3. Results and discussion

In this section, static surface pressures, as well as boundary layer data, over the wing surface, at various free stream velocities and angles of attack, are presented. The data are used to predict the transition point on the model and its variations with Reynolds number and angle of attack. Surface pressure

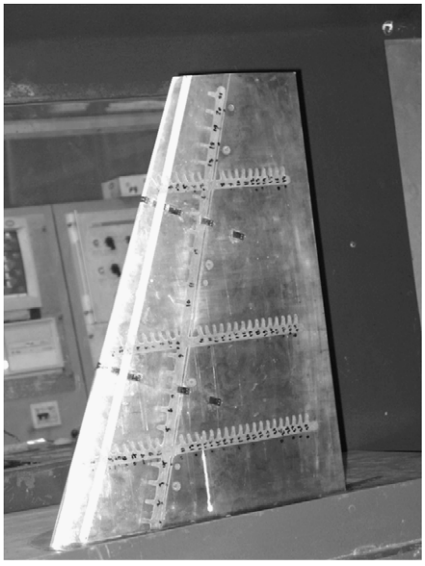

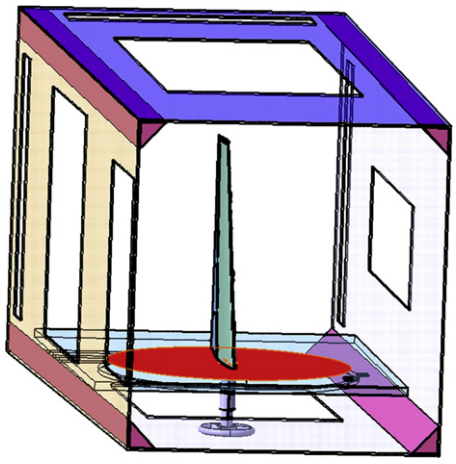

(a) The model and its schematic in the test section.

Figure 1: Schematic of the test setup and pressure orifices on the wing surface.

data are presented first, followed by those of the boundary layer.

3.1. Surface pressure results

Static pressure over the wing upper surface at Section b for various angles of attack is shown in Figure 4. The model is instrumented with three chordwise rows of pressure orifices located at the inboard section of the wing; Section a: $y/b = 0.2$ inboard section, Section b: $y/b = 0.43$ middle section, and Section c: $y/b = 0.78$ outboard station. The tests are conducted at tunnel speeds of $V_\infty = 50$–80 m/s and at angles of attack ranging from $\alpha = -2^\circ$ to 8°. Figure 4 shows the effect of angle of attack on the wing surface pressure distribution for the middle section, Section b. It can be seen by inspection that as the angle of attack increases, a suction peak over the wing surface is developed. For angles of attack of $\alpha = 4^\circ$ to 6°, the peak pressure is located at $\frac{X}{C} \cong 0.05$, and moves toward the leading edge, $\frac{X}{C} \cong 0$, for higher A.O.A., $\alpha = 7^\circ$ and 8° (Figure 4). It should be noted that the region over the wing surface, where $\frac{dC_p}{dx}$ is negative, called the favorable pressure gradient region, where the value of C_p increases negatively, is creating more suction over the wing surface. For the positive pressure gradient region, $\frac{dC_p}{dx} > 0$, $\left|C_p\right|$ decreases but the value of C_p increases positively, and is called the adverse pressure gradient.

For angles of attack in the order of $3^\circ \leq \alpha \leq 8^\circ$, the flow over the wing surface (after the suction peak) encounters a region of adverse pressure gradient, which persists to the wing trailing edge. However, the slope of C_p over the wing surface varies, as seen from Figure 4. For angles of attack of 2° and 3°, the suction peak on the C_p data cannot be distinguished. Figure 4 shows that for these angles of attack, $\left|C_p\right|$ increases from $x/c = 0$ to $x/c \cong 0.04$, and then remains almost constant up to $x/c \cong 0.45$, a region of almost constant pressure, $\frac{dC_p}{dx} \cong 0$. For $x/c > 0.45$, the flow encounters a region of adverse pressure gradient for $\alpha = 2^\circ$ and 3°, where $\left|C_p\right|$ decreases. The C_p data for other angles of attack, $-2^\circ \leq \alpha \leq 0^\circ$ degrees, show that the flow over the wing upper surface accelerates from $x/c = 0$ to $x/c \cong 0.48$, and then decelerates over the rest of the wing surface, $x/c > 0.48$. From the results, one may conclude that the flow over a significant portion of the wing surface remains laminar if the wing is flying at angles of attack of 0°–3°. However, it should be mentioned that the existence of a low suction peak in the leading edge vicinity of $\alpha = 3^\circ$, as seen in Figure 4, may trigger the boundary layer transition; in other words, the transition may occur closer to the leading edge.

For higher angles of attack, specially $\alpha > 6^\circ$, the existence of a large suction peak in the vicinity of the wing leading edge indicates that the flow becomes turbulent close to the suction peaks, $x/c > 0$. From the surface pressure data, it is seen that the flow will definitely transient to turbulent between $0 < x/c < 0.15$ for angles of attack of 7° and 8°.

The flow over the wing surface at this section (Section b) seems to be completely attached for all angles of attack shown in Figure 4, which is in agreement with the visualization results published in [17]. It should be pointed out that since the trailing edge is too thin, no pressure taps were installed for $\frac{X}{C} > 0.8$ (Figure 1(b)). In addition to the *Cp* data shown in Figure 4, the vertical line drawn through the data for $\alpha = 7^\circ$ shows the possible error due to the measurement inaccuracies. All data are corrected for a solid tunnel sidewall and for the wake blockage effects, using the method explained in [18]. Furthermore, using the method of [16], both the single sample precision and the bias uncertainty in each measured variable were estimated, and subsequently propagated into the *Cp* variations. The maximum overall uncertainty calculated in this way for the *Cp* data was less than $\pm 3\%$ of the total *Cp* values.

Figure 5 shows the effect of Reynolds number on the wing surface pressure for two different angles of attack, $\alpha = 0^\circ$ and $\alpha = 8^\circ$. It should be mentioned that the Reynolds number is changed by varying the free stream velocity. Although this method will alter the flow compressibility, since the maximum free stream velocity is $V_\infty = 80$ m/s, the aforementioned effect is negligible. From Figure 5(a), it is clearly seen that the Reynolds numbers do not have a significant influence on the wing surface pressure distribution. However, as the Reynolds number increases, a slight change in the *Cp* variations

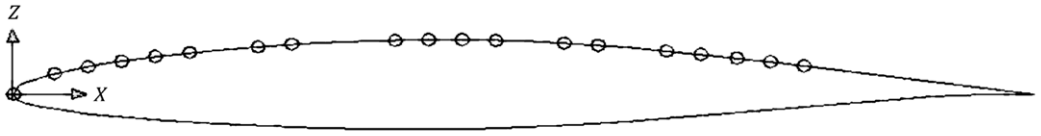

Airfoil geometry		
x/c	Z_{upper}/c	Z_{lower}/c
0.00	0.000	0.000
0.02	0.017	-0.013
0.05	0.026	-0.018
0.07	0.030	-0.021
0.09	0.035	-0.024
0.12	0.038	-0.027
0.14	0.042	-0.029
0.16	0.045	-0.031
0.19	0.048	-0.033
0.21	0.051	-0.034
0.23	0.053	-0.035
0.26	0.055	-0.037
0.28	0.056	-0.037
0.31	0.058	-0.038
0.35	0.060	-0.039
0.40	0.061	-0.039
0.45	0.061	-0.039
0.49	0.059	-0.037
0.54	0.056	-0.035
0.59	0.053	-0.032
0.65	0.047	-0.026
0.72	0.039	-0.020
0.79	0.029	-0.013
0.86	0.020	-0.007
0.92	0.010	-0.001
1.00	0.000	0.000

Pressure tabs		
Tap no.	x/c	Z_{upper}/c
1	0.00	0.000
2	0.04	0.022
3	0.07	0.031
4	0.11	0.037
5	0.14	0.042
6	0.17	0.046
7	0.24	0.053
8	0.27	0.055
9	0.38	0.060
10	0.41	0.061
11	0.44	0.060
12	0.47	0.060
13	0.54	0.057
14	0.57	0.054
15	0.64	0.048
16	0.67	0.044
17	0.71	0.040
18	0.74	0.036
19	0.78	0.032

(b) Positions of the surface pressure tabs at the midchord and the airfoil geometry.

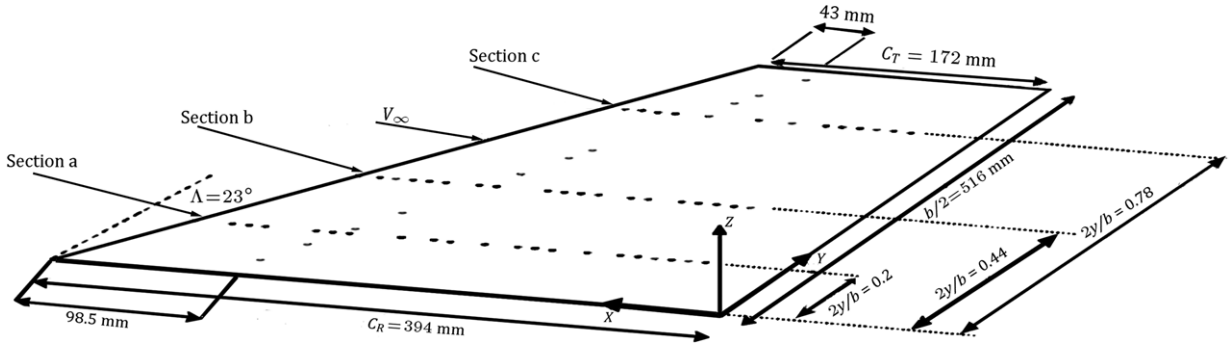

(c) Pressure orifices and the coordinate system.

Figure 1: (*continued*)

is seen from Figure 5(a). As the angle of attack is also increased to 8° (Figure 5(b)), *Cp* data for all Reynolds numbers becomes invariant. This is probably due to the fact that the flow over the entire surface becomes turbulent; hence the Reynolds number does not have a significant effect on the *Cp* data.

It is well known that in the transition region, the disorder of the flow eddies is more than that in other regions. Studies of the statistical property of the pressure signals may be used to approximately identify the transition limits. The skewness parameter is a suitable measure for indicating the level of flow disorder. In the transition region, the value of this parameter reaches to zero sharply [19]. The changes in the skewness parameter are shown in Figure 6 for pressure ports at station 2 and for three different angles of attack. As seen from Figure 6(a), the skewness parameter for the pressure port, located at $\frac{X}{C} \cong$

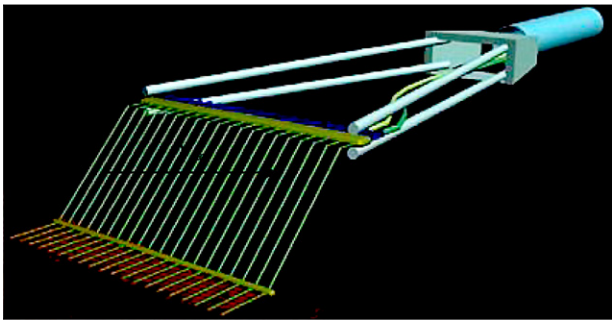

(a) Schematic view of the rake.

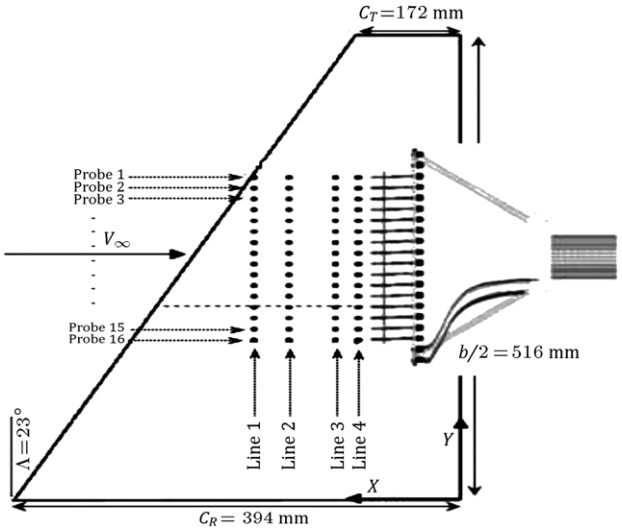

(b) Measurement positions.

Figure 2: The rake and the measurement positions on the model.

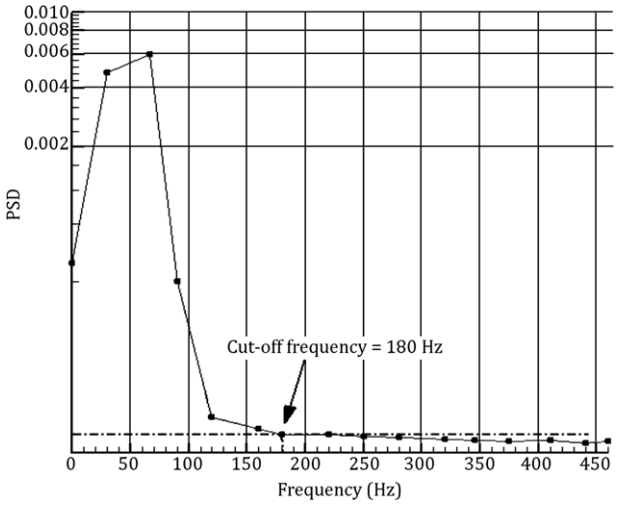

Figure 3: PSD of one channel for determining the cut off frequency.

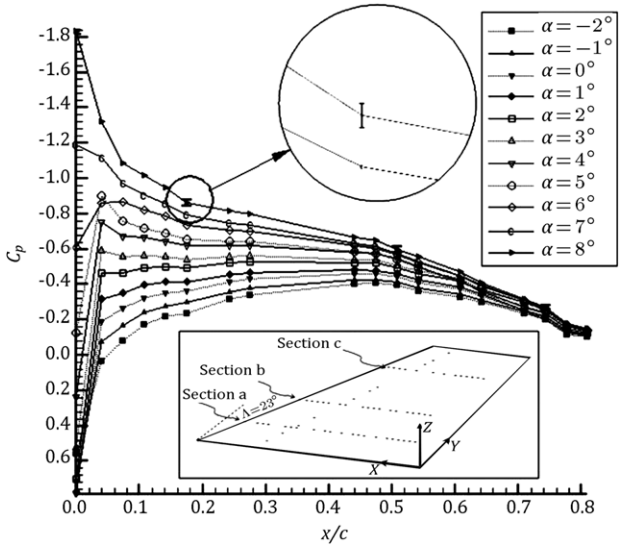

Figure 4: Effect of A.O.A on the chordwise pressure distribution; Section b, $V_\infty = 50$ m/s.

0.6 of Section b, is zero. Accordingly, this location is in the vicinity of the transition region. When the angle of attack is increased to $\alpha = 3°$ (Figure 6(b)), the transition occurs at $\frac{X}{C} \cong 0.4$. This shows that by increasing the A.O.A., the transition region moves toward the wing leading edge. However, from Figure 6(c), where the model is set to A.O.A. of 6°, it is seen that the transition point reaches $\frac{X}{C} \cong 0.03$. Therefore, it can be concluded that for this angle of attack, $\alpha = 6°$, the flow over the entire model at this section is turbulent. This conclusion is further verified in the following sections of the paper.

The change of transition point with angles of attack from the previous figures, (Figure 6(a)–(c)), is plotted in Figure 7. In addition, the transition variations with angle of attack for the other two sections, Sections b and c, which are calculated in a similar manner as Section b, are plotted in Figure 7. This figure shows that the transition point does not vary significantly with increasing the angle of attack up to $\alpha \cong 1°$, $\frac{X}{C}|_{\text{transition}} \cong 0.61$ for $0° < \alpha \leq 1°$. However, beyond this angle of attack, the $\alpha \cong 1$ transition point moves toward the leading edge abruptly.

For $\alpha > 2°$, a large portion of the wing upper surface is covered with turbulent flow (Figure 7). For the laminar flow region, $\alpha \langle 2°$ and $\frac{X}{C} \rangle 0.6$, there exist some discrepancies between the present method, the method with the skewness parameter, and the predicted data from the X-foil code [20]. The predicted data by the X-foil code indicate that the flow transits to turbulent at a slightly higher $\frac{X}{C}$, closer to the leading edge of the model. At $\alpha = 0°$, the transition point predicted by the code is located at about $\frac{X}{C} \cong 0.75$, while the one obtained through the skewness parameter indicates that the transition at this angle of attack occurs at $\frac{X}{C} \cong 0.61$. The differences are due to the 3D and instability effects that are not implemented in the X-foil code. It may be possible that the wing sweep angle forms an instability mode similar to that of the cross flow mode, which promotes the transition phenomena.

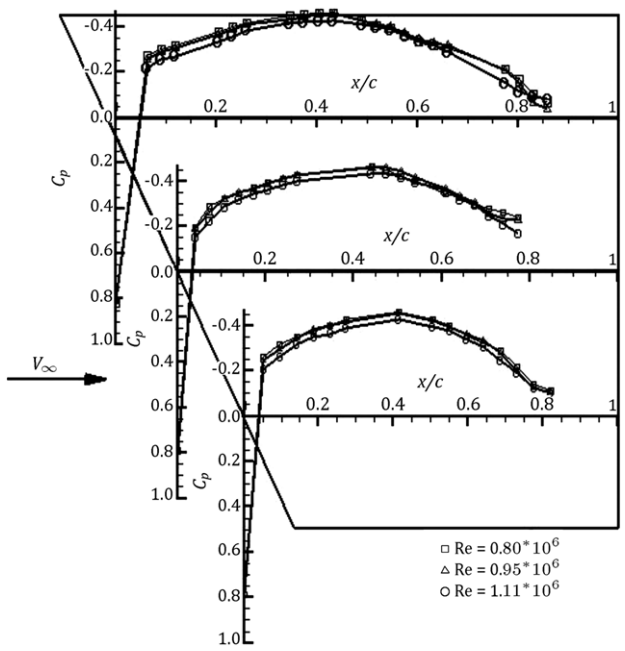

(a) $\alpha = 0°$.

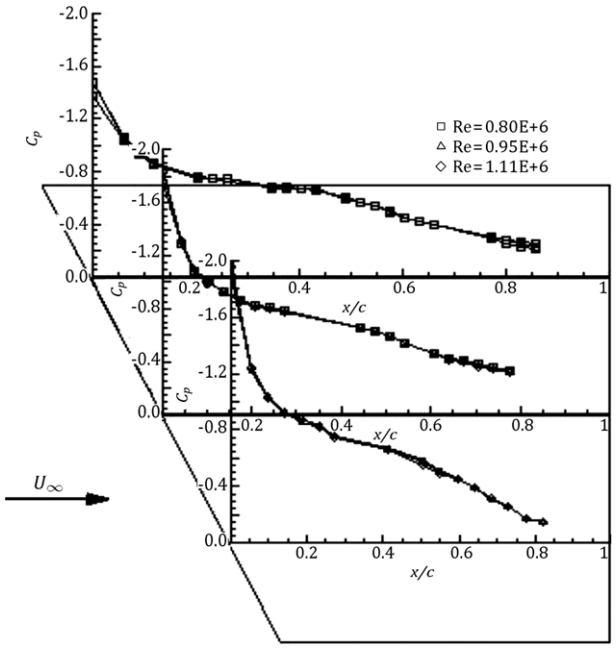

(b) $\alpha = 8°$.

Figure 5: Effect of Re on the wing surface pressure.

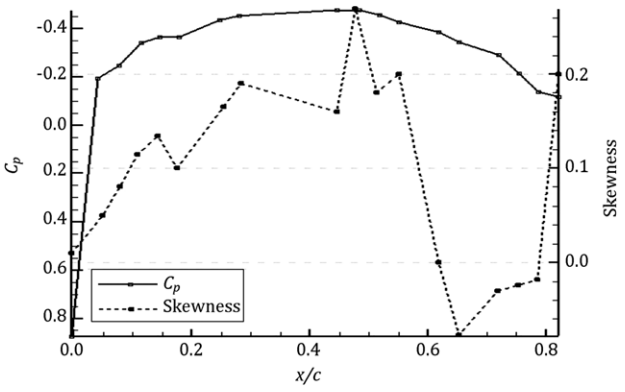

(a) $\alpha = 0°$.

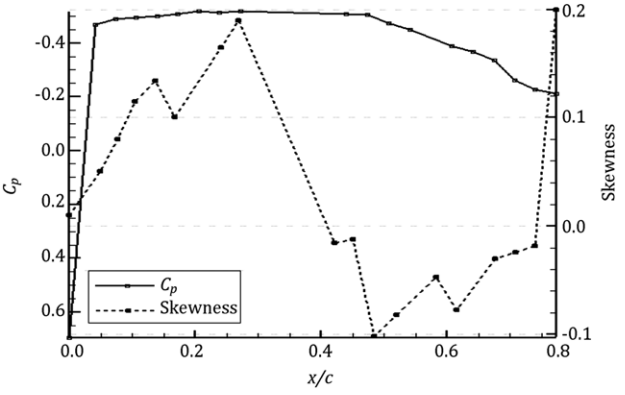

(b) $\alpha = 3°$.

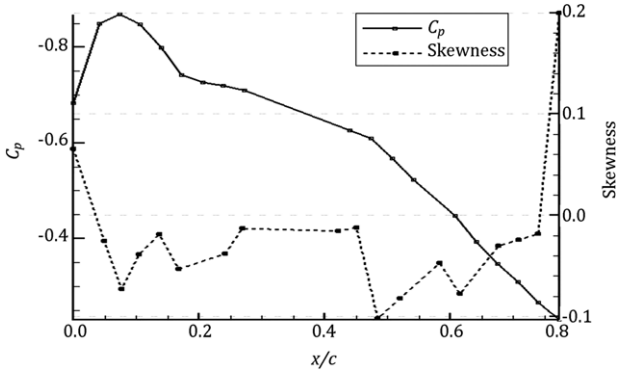

(c) $\alpha = 6°$.

Figure 6: Variations of the skewness and *Cp* with x/c for Section b.

3.2. Spectral analysis results of the pressure rake

The total pressure over the wing surface at different locations, measured with the boundary layer rake, is analyzed via the spectral method. Total pressures are measured by sensitive, high frequency pressure transducers, located at a distance of about 3 cm from the tip of the probe of the rake. The rake is moved in the z direction, as shown in Figure 2(b), from $z = 0$ up to $z = 9.8$ mm above the wing surface. During the measurement process, it is ensured that the rake is kept perpendicular to the wing surface at all z locations. Time dependent pressure data with a nominal acquisition frequency of 1 kHz are measured, and used to obtain the mean and the fluctuating pressure at each probe (Figure 2(b)). It should be mentioned that the position of each probe over the wing surface in the X, Y and Z directions was exactly known. The model is set to zero degree angle of attack, and the free stream velocity is maintained at $V_\infty = 50$ m/s. By analyzing the data, one may observe the growth of the instability, hence the appearance of the disturbed flow. This is done by taking the Fourier transformation of the signals and examining the kinetic energy level in the data. For this purpose, the spectrum is calculated for the pressure signals at all positions shown in Figure 2(b). At each measurement position, the fluctuating outputs are measured and filtered, as explained previously.

Figure 8 shows the pressure fluctuation spectra at position 1, probe 1. Total pressure data are taken at four different z locations over the wing surface, $z = 0$–9.8 mm. It can be seen from this figure that the fluctuation levels are extremely low. However, several features are detected from the data. First, the largest disturbances are approximately between the frequencies of 85 and 115 Hz. These fluctuations are the largest traveling crossflow waves. Second, there exists another relatively large fluctuation near the frequency of $F = 150$ Hz. This fluctuation may be due to the TS waves that exist despite the favorable pressure gradient in this region of the model that is in the vicinity of the leading edge (Figure 2(b)). All flucuations decrease as the distance from the body is increased (z increases from zero to 9.8 ss).

Figure 9 shows the perturbation energy level in the boundary layer over the wing surface for a few points, probe 1 through probe 16. It should be noted that as shown in Figure 2(b), the pressure rake has 16 total pressure probes and is moved over the wing surface from $z = 0$ to $z = 9.8$ mm at four different $\frac{X}{C}$ positions (referred to as line 1 through line 4 in this paper). The data shown in Figure 9 are for line 1, as shown in the top of the figure. However, due to the large number of probes, 16 of them, the data for only 6 probes are shown in Figure 9. The data are plotted as the calculated PSD vs. the dominant frequencies for each probe. The dominant frequencies are determined for all probes in a way similar to that outlined previously (Figure 8). The variation of the PSD vs. frequency for probe 1 located on line 1 is shown in Figure 8; the dominant frequencies were discussed previously. From Figure 9, it is clearly seen that for dominant frequencies of 89, 100, and 111 Hz, the calculated PSD for probe 1 through probe 16 increases. This indicates that with respect to the locations of the corresponding probes (top of Figure 9), as both $\frac{2y}{b}$ decreases (moving closer to the wing root) and $\frac{X}{C}$ increases (moving farther away from the wing leading edge), the amplitude of the perturbation, PSD, increases. This increase is due to the perturbation in the boundary layer away from the wing leading edge and the wing sweep effect. However, for the dominant frequency of 149 Hz, the PSD first increases, and then as the distance between the root and the point of measurement decreases, the calculated PSD decreases (Figure 9). The calculated PSD for probes 12 and 13 for the dominant frequency of 149 Hz are higher than the PSD's for other probes. If one relates this frequency, 149 Hz, to the TS instability modes, as seen and discussed from Figure 8, one may hypothesize that the reductions of the PSD for probe numbers 15 and 16 are due to the interaction of the crossflow and the aforementioned frequency.

As mentioned before, by relating the amplitude of the frequency of 149 Hz with the TS instability modes, it would be helpful to study the PSD variations for this frequency over the selected wing surface area for different probes of the total pressure rake. The data for the selected number of probes, probe numbers 1, 2, 13, and 16, are shown in Figure 10(a) for $f =$

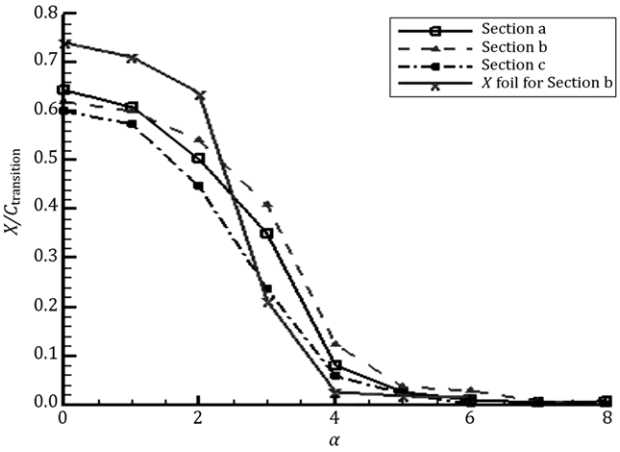

Figure 7: Comparison of the transition point from the skewness data for three sections; $V_\infty = 50$ m/s.

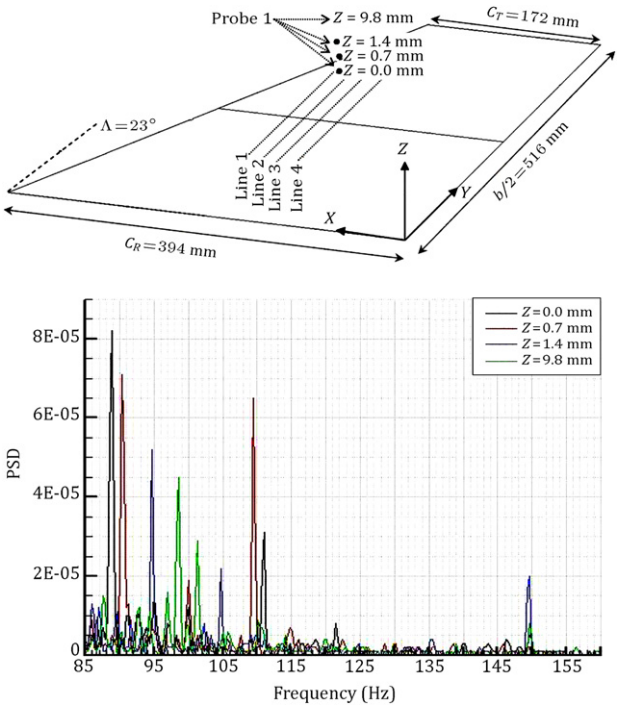

Figure 8: Comparison of the measurement signals at position 1 for different Z locations; $\alpha = 0°$, $V_\infty = 50$ m/s.

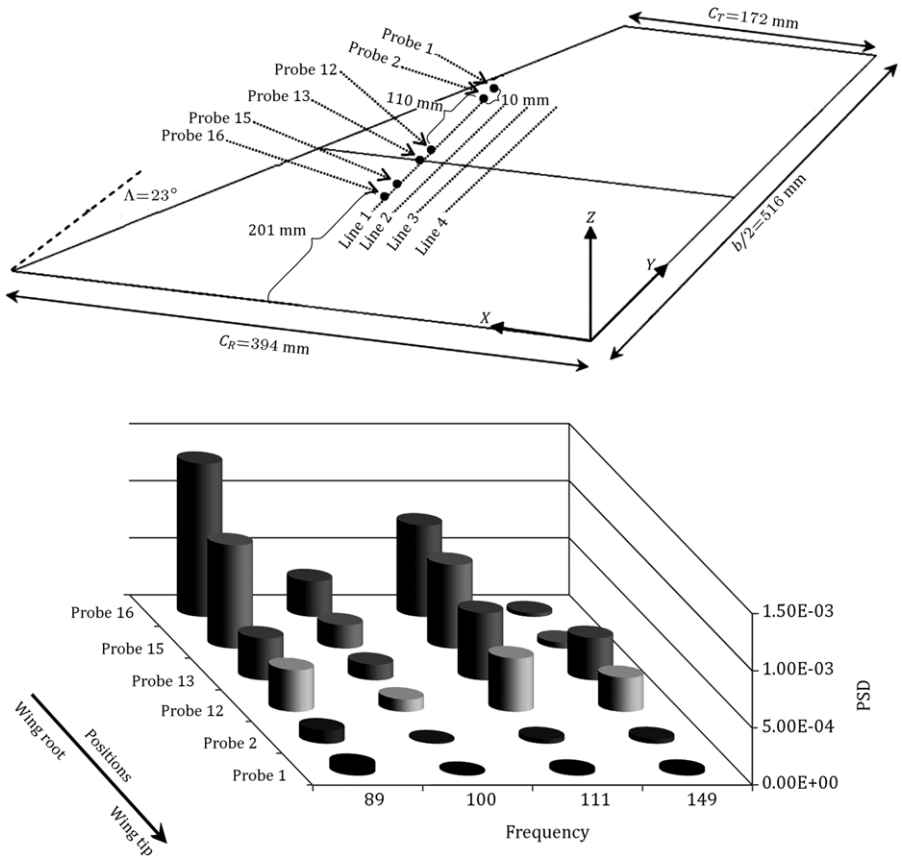

Figure 9: Variations of the calculated PSD over the wing surface with dominated frequency; $\alpha = 0^\circ$, $V_\infty = 50$ m/s.

149 Hz. It should be taken into consideration that the calculated PSD's are for different $\frac{X}{C}$'s (top of Figure 10(a)). As indicated previously, at each $\frac{X}{C}$'s (four of them), the 16 probe rake was moved perpendicular to the wing surface in the z direction from $Z = 0$ to $Z = 9.8$ mm. The corresponding data are then filtered, and the spectrum for each probe is calculated. For all PSD data shown here, the model is set to zero degrees angle of attack, and the free stream velocity is $V_\infty = 50$ m/s. From Figure 10(a), it is clearly seen that the amplitude of the disturbances, PSD, for each probe increase as $\frac{X}{C}$ increases, moving from the L.E. toward the T.E., shown at the top of Figure 10(a). However, for all $\frac{X}{C}$'s, the calculated PSD for line number 4, closer to the model T.E., decreases, which is due to the turbulent flow in this region.

Furthermore, Figure 10(a) clearly shows that the calculated spectra across all lines increase as $\frac{2y}{b}$ decreases, i.e the disturbances over wing surface increases from the tip toward the root section of the wing. However, close to the root section, the disturbances decrease (spectra of probe number 16). It should be pointed out that along each line, as $\frac{2y}{b}$ decreases, $\frac{X}{C}$ decreases too. From Figure 10(a) and the measured data, it is seen that the maximum disturbances occur where probe number 13 is located. The aforementioned comparisons are for the sections of the model that are located at $\frac{2y}{b} = 0.39, 0.44$ and 0.6. Close agreements of the measured and predicted data (2D for this section, i.e. Section b) indicate that the flow at this station behaves nearly as a 2D flow. Away from this station, the flow behavior varies, and hence the disturbances will also alter. By close examination of the PSD data shown in Figure 10(a), it can be concluded that for the frequency of 149 Hz, the amplitude of the disturbances away from the 2D section, Section b, are much smaller. However, closer to the wing root section, the amplitudes of the disturbances are much higher than locations away from it.

Figure 10(b) shows similar variations to those of Figure 10(a), but for a frequency of 111 Hz. It should be noted that for all data shown in Figure 10, the probe is located at $z = 0$ mm. This frequency, 111 Hz, is related to the crossflow instabilities. Again, it is seen that the disturbances along each line, lines 1 through 4, shown in Figure 10, increases as $\frac{2y}{b}$ decreases, moving closer to the wing root and moving away from the wing leading edge. As seen from Figure 10(b), maximum PSD occurs for probe number 16, which is located closer to the wing root section for all lines. This indicates that the cross flow instabilities are higher in this region, which is in contrast to the data shown in Figure 10(a), which are for instabilities related to the frequency of 149 Hz. Note that the data for Figure 10(b) are for the frequency of 111 Hz. In addition, the magnitude of the maximum PSD's for the frequency of 111 Hz (Figure 10(b)) are higher than those of the 149 Hz, shown in Figure 10(a). Moreover, it is seen by inspection that the magnitude of the PSD's for probe 1 is the largest. Figure 10(c) shows variations of the calculated PSD's over the wing surface for the frequency of 89 Hz. As seen from this figure, the maximum values of the PSD for all probes are much higher than the corresponding values, but at higher frequencies, 111 and 149 Hz, as shown in Figure 10(a) and (b). However, variations of the PSD's shown in Figure 10(c) are similar to those of the previous figures. Nevertheless, for probe number 16 which is located closer to the wing root, in comparison with other probes, the instabilities increase as $\frac{X}{C}$ increases, moving toward the wing trailing edge (Figure 10(c)). At 111 Hz, Figure 10(b), the PSD data for probe 16 are almost constant for all positions and for lines 1 through 4.

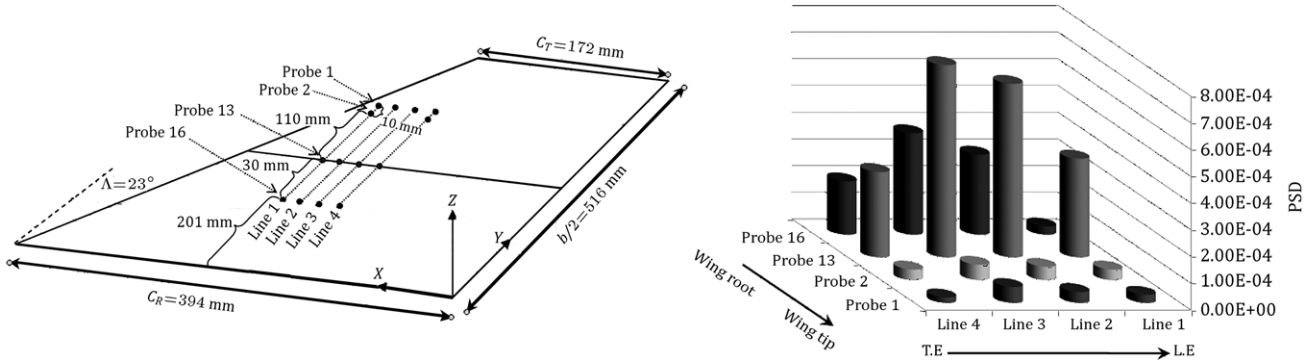

(a) $F = 149$ Hz.

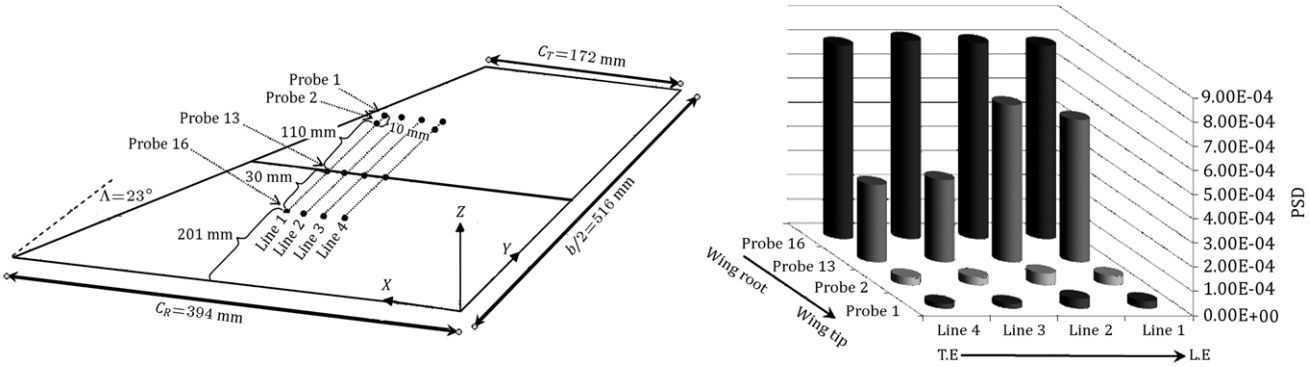

(b) $F = 111$ Hz.

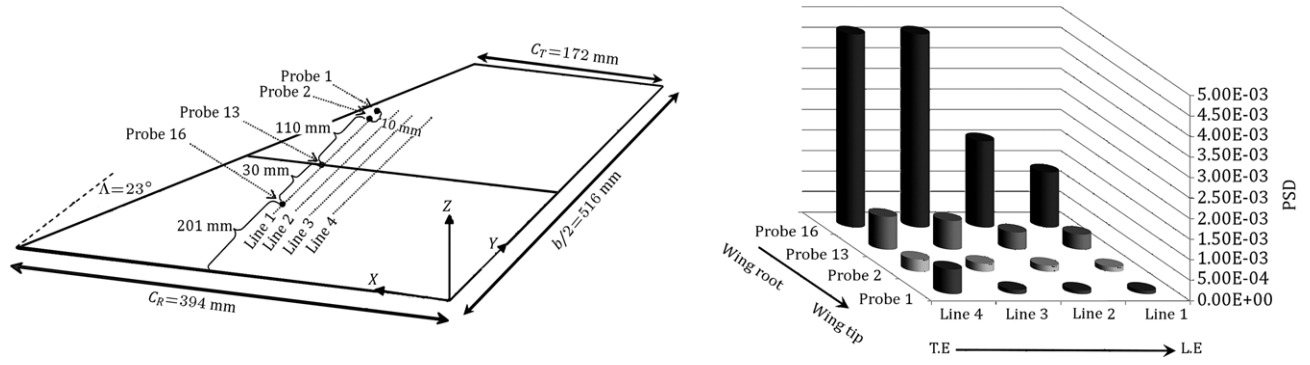

(c) $F = 89$ Hz.

Figure 10: Variations of the calculated PSD over the wing surface; $\alpha = 0^\circ$, $V_\infty = 50$ m/s.

4. Conclusion

Wind tunnel tests are performed to examine the flow field over a semi-span swept wing under various conditions. Surface pressure distribution data are obtained to predict the transition point at each chordwise section by computing the standard deviation of the pressure data. Vanishing of the skewness parameter for the pressure data indicates a transition region. A comparison of the transition point on the wing surface for three sections shows reasonable agreement for small angles of attack.

Analysis of the total pressure over the wing surface is done by taking the Fourier transformation of the signals and by examining the kinetic energy level in the data. The results indicate the influence of cross-flow and TS instabilities on the dominated boundary layer frequency. The largest disturbances are approximately between the frequencies of 85 and 115 Hz. These fluctuations are the largest traveling crossflow waves. The fluctuation with frequency of 149 Hz might be due to the TS waves that are excited, despite the favorable pressure gradient in the measured region. The amplitude of the disturbances, PSD, for each probe is increased as $\frac{X}{C}$ is increased, moving from the L.E. toward the T.E. closer to the wing root section, and their values are much higher than the corresponding values measured at locations farther from the tip of the wing.

Since the wing shape is a finite swept wing, tip vortices have an influence on instability modes. Consequently, it is necessary to use the infinite swept wing by placing a flat plate on the wing tip for reducing the effect of tip vortices and comparing the results to recent work. Further experiments should be performed to determine the interaction between the crossflow and TS waves. Obviously, this requires the knowledge of the freestream condition of the tunnel.

References

[1] Ray-Sing, L. "Stationary crossflow instability on an infinite swept wing", Ph.D. Thesis, Arizona State University, 9237268 (1992).

[2] Gray, W.E. "The effect of wing sweep on laminar flow", *RAE TM Aero* 256 (1952).

[3] Gray, W.E. "The nature of the boundary layer flow at the nose of a swept wing", *RAE TM Aero* 256 (1952).

[4] Gregory, N., Stuart, J.T. and Walker, W.S. "On the stability of three-dimensional boundary layers with application to the flow due to a rotating disc", *Phylosophical Transactions of the Royal Society London* (1955).

[5] Poll, D. "Some observation of the transition process on the windward face of a long yawed cylinder", *Journal of Fluid Mechanic*, 150, pp. 329–356 (1985).

[6] Arnal, D. and Casalis, G. "Laminar-turbulent transition prediction in three-dimensional flows", *Progress in Aerospace Sciences*, 36(2), pp. 173–191 (2000).

[7] Michel, R., Arnal, D., Coustols, E. and Juillen, J.C. "Experimental and theoretical studies of boundary layer transition on a swept infinite wing", IUTAM Symp., Novosibirsk (1984).

[8] White, E.B. and Saric, W.S. "Stages of swept-wing transition", *39th Aerospace Sciences Meeting and Exhibit*, AIAA Paper No. 2001-0271, (2001).

[9] Saric, W.S. and Reed, H.L. "Transition mechanisms for transport aircraft", *38th Fluid Dynamics Conference and Exhibit*, AIAA Paper No. 2008-3747, (2008).

[10] Anderson, B.T. and Mayer, R. "Effect of wing sweep on boundary-layer transition for a smooth F-14A wing at mach numbers from 0.7 to 0.825", *NASA Technical Memorandum*, p. 101712 (1990).

[11] Kachanov, Y.S. "Experimental studies of three-dimensional boundary layers", AIAA Paper No. 96-1978 (1996).

[12] Arnal, D., Casalis, G., Reneaux, J. and Cousteix, J. "Laminar-turbulent transition in subsonic boundary layers: research and application in France", AIAA Paper No. 97-1905 (1997).

[13] White, E.B., Sari, W.S., Gladden, R.D. and Gabet, P.M. "Stage of swept-wing transition", *39th Aerospace Sciences Meeting & Exhibit*, Reno, Nevada, AIAA Paper No. 2001-0271 (2001).

[14] Howard, R.M., *Principles of Random Signal Analysis and Low Noise Design*, John Wiley & Sons, Inc., Publication (2002).

[15] Seraudie, A., Perraud, J. and Moens, F. "Transition measurements and analysis on a swept wing in high lift configuration", *Aerospace Science and Technology*, 7(8), pp. 569–576 (2003).

[16] Thomas, G.B., Roy, D.M. and John, H.L.V., *Mechanical Measurements*, fifth ed. Addison-Wesley Publishing Company (1993).

[17] Soltani, M., Masdari, M., Seidjafari, M. and Ghorbanian, K. "Wind tunnel investigation of pressure distribution and transition position of a swept 3D wing", Accepted for publication in Journal of Aerospace Science, JAST Journal, 7 (2), pp. 132–137 (2010).

[18] Barlow, J.B., Rae, W.H. and Pope, A., *Low Speed Wind Tunnel Testing*, third ed., John Wiley & Sons (1999).

[19] Meijering, A. "Experimental analysis of separated transitional transonic airfoil flow", *31st AIAA Fluid Dynamics Conference & Exhibit*, AIAA Paper No. 2001-2987, Germany (2001).

[20] Drela, M. "An analysis and design system for low Reynolds number airfoils", *Conference on Low Reynolds Number Airfoil Aerodynamics*, University of Notre Dame (1989).

Mohammad Reza Soltani has a Ph.D. degree in Aerodynamics from the University of Illinois at Urbana-Champaign, USA, and is now Professor in the Aerospace Engineering Department of Sharif University of Technology, Tehran. His research interests include applied aerodynamics, unsteady aerodynamics wind tunnel testing, wind tunnel design, and data processing.

Kaveh Ghorbanian obtained a Ph.D. degree in Propulsion & Combustion from the Department of Mechanical Engineering at the University of Washington, USA, in 1993, and is now Professor in the Aerospace Engineering Department of Sharif University of Technology, Tehran. His research interests include turbomachinery, thermo-acoustics, gas dynamics, and energy conversion systems.

Mehran Masdari received a B.S. degree in Aerospace Engineering and an M.S. degree in Aerodynamics from Sharif University of Technology in 2000 and 2003, respectively, and is now a Ph.D. student of Aerodynamics in the same university. His research interests include applied aerodynamics, wind tunnel testing, neural network and data processing.